

Retrospective study comparing model-based deformation correction to intraoperative magnetic resonance imaging for image-guided neurosurgery

Ma Luo
Sarah F. Frisken
Jared A. Weis
Logan W. Clements
Prashin Unadkat
Reid C. Thompson
Alexandra J. Golby
Michael I. Miga

Retrospective study comparing model-based deformation correction to intraoperative magnetic resonance imaging for image-guided neurosurgery

Ma Luo,^{a,*} Sarah F. Frisken,^b Jared A. Weis,^c Logan W. Clements,^a Prashin Unadkat,^b Reid C. Thompson,^d Alexandra J. Golby,^b and Michael I. Miga^{a,d,e,f}

^aVanderbilt University, Department of Biomedical Engineering, Nashville, Tennessee, United States

^bBrigham and Women's Hospital, Department of Radiology, Boston, Massachusetts, United States

^cWake Forest School of Medicine, Department of Biomedical Engineering, Winston-Salem, North Carolina, United States

^dVanderbilt University Medical Center, Department of Neurological Surgery, Nashville, Tennessee, United States

^eVanderbilt University Medical Center, Department of Radiology and Radiological Sciences, Nashville, Tennessee, United States

^fVanderbilt University, Vanderbilt Institute for Surgery and Engineering, Nashville, Tennessee, United States

Abstract. Brain shift during tumor resection compromises the spatial validity of registered preoperative imaging data that is critical to image-guided procedures. One current clinical solution to mitigate the effects is to reimage using intraoperative magnetic resonance (iMR) imaging. Although iMR has demonstrated benefits in accounting for preoperative-to-intraoperative tissue changes, its cost and encumbrance have limited its widespread adoption. While iMR will likely continue to be employed for challenging cases, a cost-effective model-based brain shift compensation strategy is desirable as a complementary technology for standard resections. We performed a retrospective study of $n = 9$ tumor resection cases, comparing iMR measurements with intraoperative brain shift compensation predicted by our model-based strategy, driven by sparse intraoperative cortical surface data. For quantitative assessment, homologous subsurface targets near the tumors were selected on preoperative MR and iMR images. Once rigidly registered, intraoperative shift measurements were determined and subsequently compared to model-predicted counterparts as estimated by the brain shift correction framework. When considering moderate and high shift (>3 mm, $n = 13 \pm 6$ measurements per case), the alignment error due to brain shift reduced from 5.7 ± 2.6 to 2.3 ± 1.1 mm, representing $\sim 59\%$ correction. These first steps toward validation are promising for model-based strategies. © 2017 Society of Photo-Optical Instrumentation Engineers (SPIE) [DOI: 10.1117/1.JMI.4.3.035003]

Keywords: brain shift; image-guided neurosurgery; registration; finite element; deformation; computational modeling.

Paper 17102PR received Apr. 17, 2017; accepted for publication Aug. 21, 2017; published online Sep. 13, 2017.

1 Introduction

Surgical resection via image-guided neurosurgery (IGNS) is a standard of care for patients with brain tumors. By coregistering the patient space to high-resolution preoperative magnetic resonance (MR) imaging, surgeons can better localize tumor regions, assess tumor margins during resection, identify eloquent functional areas to avoid, and navigate in the surgical field. Thus, the quality and safety of the resection procedure heavily rely on the agreement between the preoperative MR image registered to the patient space and the patient's intraoperative anatomy. This agreement, however, can be compromised when brain shift, i.e., soft tissue deformation, occurs during surgery. Studies have reported cortical surface shifts up to 24 mm and subsurface shift ranging between 3 and 7 mm.^{1–4}

Brain shift is a complex spatiotemporal event caused by a number of contributing factors, such as cerebrospinal fluid (CSF) drainage, the administration of osmotically active drugs, swelling, and resection effects.^{2,4–8} Intraoperative imaging is a direct method to visualize and assess brain deformation. Ultrasonography (US), computed tomography (CT), and MR are the commonly utilized intraoperative imaging modalities to monitor brain shift. However, due to poor soft tissue contrast in both CT and US in comparison to intraoperative MR (iMR),

limited volumetric information provided in US, as well as the risk of radiation exposure in CT, iMR imaging has emerged as the most widely adopted option to compensate for brain shift intraoperatively.^{1,4,5,9,10}

The implementation and practice of iMR imaging have shown considerable positive effects in clinical outcome. For example, in a 200-patient study by Nimsy et al.¹¹ using iMR techniques for a variety of neurosurgical operations, it was found that iMR had immediate procedural impact in 27.5% of cases (e.g., further resection when incomplete tumor removal was revealed on iMR imaging). More recent studies by Senft et al.¹² and Schulz et al.¹³ have further demonstrated that in a significant portion of brain tumor resection cases, intraoperative updating of the preoperative diagnostic imaging data to account for soft tissue changes is valuable and is needed. However, iMR, the widely accepted clinical and commercial option at this time, has had limited adoption due to cost and encumbrance considerations.^{3,11} As a result, computational model-based brain shift compensation strategies designed to realign the preoperative MR image to the patient's intraoperative anatomy using sparse, accessible, and readily acquired intraoperative data may provide a cost-effective and complementary means to compensate for soft tissue deformation.

*Address all correspondence to: Ma Luo, E-mail: m.luo@vanderbilt.edu

There have been several research efforts in the development of predictive biomechanical modeling, driven by sparse intraoperative data, to compensate for brain shift. However, the main challenge associated with computational model-based approaches is the difficulty of validating the proposed methods. As a preliminary validation step, a number of studies have employed physical or digital phantoms to assess the accuracy of their proposed brain shift correction algorithms.¹⁴⁻¹⁶ The advantage of using phantoms is that it is highly controlled and allows for detailed comparisons. However, phantom testing environments lack soft tissue equivalence and do not incorporate the heterogeneous nature of their *in vivo* counterparts.¹⁴

Another approach for evaluating the efficacy of brain shift correction frameworks, proposed by Dumpuri et al.,¹⁷ is a retrospective comparison study analyzing the shifts of homologous feature targets, measured with preoperative and postoperative MR images, versus model-predicted displacements.⁴ While the utilization of postoperative MR images provides a more realistic and clinically relevant assessment of the performance of model-based brain shift correction algorithm, brain shift measured from postoperative MR was shown to be less pronounced when compared to intraoperative brain shift. More specifically, in the follow-up work by Chen et al.,¹⁸ when comparing intraoperative cortical surface shift to that of the pre- and postoperative study of Dumpuri et al.¹⁷ for the same patients, the study found that between the intraoperative and postoperative imaging presentations, the cortical surface shift could recover as much as 35% to 65% of its intraoperative shift. The differences likely stem from the natural replenishment of CSF postoperatively with subsequent restoration of buoyancy forces and potential difference in head orientation between surgery and postoperative imaging. These studies also further demonstrate the highly dynamic nature of brain shift.

While the studies above provide insight on the feasibility of employing a model-based approach for intraoperative brain shift compensation, the ideal strategy for assessment is to establish measurements of brain shift using iMR technology and then compare the measurements to model-based predictions. Several teams have attempted to compare model-based approaches with iMR for validation. Skrinjar et al.¹⁹ presented an early attempt to use iMR to validate the brain shift recovery efficacy of a continuum mechanics-based model in two patient cases, with 14 landmarks in each case. Another early attempt to use iMR for model performance validation was performed by Ferrant et al.,²⁰ who evaluate the accuracy of their model by tracking 400 landmarks in five intraoperative scans acquired successively, where the landmarks are placed in both hemispheres of the brain. Zhang et al.²¹ have also taken the iMR approach to validate their linear elastic model-based brain shift correction strategy, which is driven by imposing the cortical surface deformation, acquired intraoperatively via laser range scanner (LRS), as boundary conditions. Five patients were selected for the Zhang et al.²¹ study and four to six landmarks are identified in each case, totaling 25 landmarks, with a mixture of locations near the tumor, in mid volume, and on the cortical surfaces. Joldes et al.²² also employ iMR to validate their biomechanical model in five patient cases, using the misalignment of the three-dimensional (3-D) bounds of the ventricles between the intraoperative segmentations and model predictions, rather than anatomical landmarks, to provide an understanding of model accuracy. Another group that has used iMR to assess their model-based method is Vigneron et al.²³ They similarly chose not to use tissue landmarks for validation in two patient cases analyzed, but rather implemented a modified Hausdorff distance metric where they compare the edge maps extracted via Canny method from the original, intraoperative, and model deformed image volumes in the whole brain, as well

Table 1 Reported results and findings in selected literatures—validation of model-based approaches with iMR.

Reference	Validation metric	Results and findings
Skrinjar et al. ¹⁹	$N = 2$; 14 landmarks in each case, throughout the volume of the cerebral hemisphere, away from the exposed brain surface, on the side of craniotomy.	Maximal landmark displacement is 3.8 mm; maximal error of the predicted brain deformation is 1.4 mm.
Ferrant et al. ²⁰	$N = 1$; with a sequence of five successive intraoperative scans; a total of 400 landmarks placed in both hemispheres: 37% in boundary surfaces (16% on the ventricles and 21% on the cortical surface), 41% in mid volume, and 22% in tumor and resection regions.	Average displacement of all landmarks before and after deformation modeling is reduced from 1.7 to 0.9 mm (for surface landmarks: 1.6 to 0.7 mm, for mid volume: 1.6 to 0.9 mm, and for tumor region: 2.3 to 1.6 mm).
Zhang et al. ²¹	$N = 5$; a total of 25 landmarks: 19 near tumor, 4 in mid volume, 2 on cortical surface.	For all landmarks, measured displacement is 3.9 ± 2.8 mm and error is 1.2 ± 0.6 mm. For landmarks near the tumor, measured displacement is 4.2 ± 3.1 mm and error is 1.25 ± 0.6 mm.
Joldes et al. ²²	$N = 5$; 3-D bounds of the ventricles.	The maximum errors were 1.6 mm in the medial-lateral direction, 1.6 mm in anterior-posterior direction, and 2.2 mm in inferior-superior direction in predicting intraoperative bounds of the ventricles between intraoperative segmentations and model predictions.
Vigneron et al. ²³	$N = 2$; modified Hausdorff distance in the whole brain, as well as in the region and neighborhood of the tumor.	For the whole brain, the modified Hausdorff distance decreased from 1.24 to 1.08 mm in one case and increases from 1.01 to 1.04 mm in the other case before and after model intervention. The modified Hausdorff distance decreases from 1.36 to 1.28 mm in the region and neighborhood of the tumor.

as in the tumor region and its neighborhood, as confirmation that their model was able to better realign the preoperative imaging data with patient intraoperative anatomy.²³ Results and critical findings of these studies are summarized in Table 1.

These iMR validation studies have further demonstrated the viability of employing biomechanical models to predict brain shift intraoperatively. However, small sample sizes in these studies—in both the number of patients and the number of landmarks investigated near the tumor region, which are of significant interest to the surgeons—provide more impetus for studies using iMR as a brain shift comparator for model-based shift correction in tumor resection surgeries.

We have developed a brain shift correction framework that uses a biphasic biomechanical modeling approach to construct a deformation atlas of potential deformation solutions precomputed based on variables associated with potential surgical presentations of the patient in the operating room.^{2,18,24–26} Intraoperatively, the approach is driven by sparse cortical surface deformation data. Subsequently, intraoperative volumetric brain shift is estimated with an inverse problem approach, whereby a combination of atlas solutions is drawn from the suite of precomputed deformation solutions to best-fit the intraoperative surface data. Once complete, the model-derived deformation field may be applied to the preoperative MR imaging to reflect the predicted volumetric brain shift during surgery, thus improving the precision of IGNS.

This study represents our continuing effort to validate the developed brain shift correction strategy and is the latest advancement toward a more comprehensive and prospective validation fidelity study in the near future. The objective of this study is to assess the overall performance of our methodology by analyzing subsurface landmarks with moderate and high shift (above 3 mm) near tumor resection regions and compare with the state-of-the-art clinical iMR technology.^{10,27}

2 Methods

A semiautomated computational framework, built on a biphasic biomechanical model, for brain shift correction has been realized.² Preoperative and intraoperative imaging data of nine patients have been acquired to assess the extent of brain shift during tumor resection surgery. All patients provided written consent prior to imaging for this Brigham and Women's Hospital Institutional Review Board approved study.

In this retrospective study, the data have been used to drive our brain deformation correction framework, and comparisons of brain shift between iMR measurement and model prediction have been performed. The overall workflow of this comparison study with iMR is shown in Fig. 1.

Briefly, in the preoperative routine shown in Fig. 1, a patient's preoperative MR image volume is obtained prior to surgery. Within a previously developed model framework, a series of preoperative computing steps are performed beginning with segmentations of the patient's brain, tumor, tentorium cerebelli, falx cerebri, and brain stem.²⁵ From the segmented volume, a patient-specific finite-element mesh is generated. A preoperative surgical plan is determined by the surgeon, which includes an approximation to the anticipated head orientation, the location, and approximate size of the craniotomy. This information is then provided to an automatic boundary condition generator that systematically produces a suite of boundary conditions that capture anticipated variability of patient's surgical presentation within the procedure.^{2,26} Once complete, the

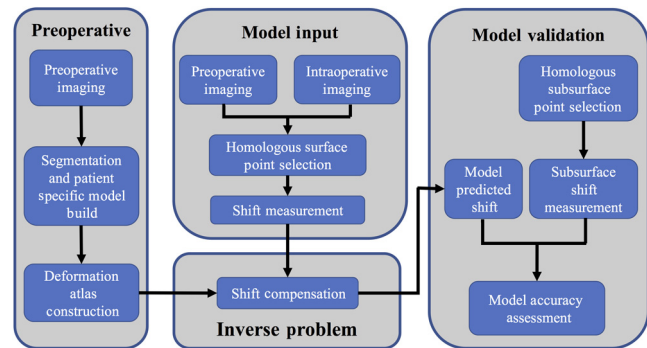


Fig. 1 Overall workflow of the comparison study with iMR in evaluating a deformation atlas-based brain shift correction framework.

boundary conditions are used within the context of an existing biphasic soft tissue finite-element model to generate a distribution of possible volumetric deformation solutions that capture a range of anticipated brain shifts due to gravitational sag, hyperosmotic drugs, tissue swelling, and resection cavity effects, in a so-called “deformation atlas.”

Intraoperatively, cortical surface deformation is measured, and a constrained combination of solutions from the deformation atlas is produced to best match cortical surface shift via an inverse problem as shown in Fig. 1. This combination of solution represents the model-predicted brain shift intraoperatively.

For this retrospective study, the sparse input data used to drive the inverse problem are the measured cortical surface deformation (shown in the model input block of Fig. 1), which is obtained by extracting homologous cortical surface points from the MR image volumes. More specifically, preoperative MR and iMR image volumes were rigidly registered. We note here that this registration has to be taken with care in that it requires the registration of geometrically consistent features, e. g., skull. A general intensity-based registration of the brain tissue itself for example would be inappropriate given that the intraoperative and preoperative presentations of the tissue are quite different. More specifically, deformations measured to drive the pipeline must reflect displacement trajectories relative to the preoperative state, not necessarily the best rigid alignment of brain tissue intensities. Frameworks that work on a biophysical simulation basis, such as the one in this work, require this type of control. Fortunately, in the operating room, the initial registration of a patient and subsequent attachment of a reference target to that configuration are the standard of care. Interestingly, it is only within the iMR validation environment that this challenge appears but certainly is worth noting here. Nevertheless, to assess in this work, relatively rigid structures, such as the skull and/or orbits, were used to establish this registration reference for quality assurance.

Once rigidly registered, using 3-D Slicer²⁸ and Analyze 9.0 (AnalyzeDirect, Overland Park, Kansas), homologous surface feature points around the surgical site on the preoperative and registered intraoperative images were determined, and differences in position between the corresponding feature points served as our measurement of intraoperative cortical surface deformation. After cortical surface shift was determined, surface deformations only were used to drive the correction algorithm via our inverse problem approach, i.e., an optimal combination of precomputed deformation atlas solutions produced to best match the measured surface deformation. Once achieved, the preoperative MR image could then be updated based on the

aforementioned optimal volumetric deformation solution. We should further note that while the deformation atlas contains solutions with and without resected tumor volume influences, intratumor volume displacements are interpolated based on the combination of solutions. More specifically, we have found that interpolating intratumor intensity content from the preoperative image, rather than placing a void, is a preferred visual assessment.¹⁷

Last, for model validation in Fig. 1, the quality of the model correction was assessed by examining the differences between measured subsurface shift and model-predicted subsurface shift near the tumor region, as evaluated by determining the shift in homologous subsurface feature points designated between preoperative and intraoperative images and comparing to those determined from the computational model. We should emphasize that the homologous subsurface measurements were used solely to assess the fidelity of our corrections and not used in any way to drive the inverse problem framework.

2.1 Preoperative Image Information and Segmentation

Preoperative MR and iMR images were acquired for nine patients at Brigham and Women's Hospital (Boston, Massachusetts). The intraoperative scans are acquired by a high-performance high-field (3 T) wide bore (70 cm) MRI scanner (Siemens Magnetom Verio, Erlangen, Germany). Details of the patient information can be found in Table 2.

The specification of the preoperative MR and iMR images, namely, the voxel spacing and the selection of MR sequence, was case specific. Details of the preoperative MR and iMR images of each patient can be found in Table 3.

For each patient, the patient's brain and tumor were manually segmented via ITK-SNAP.²⁹ To facilitate automatic segmentation of dural septa, the patient's brain was rigidly and nonrigidly

registered to an expert segmented atlas image set with dural septa presegmented using a normalized mutual information algorithm and the adaptive bases algorithm, respectively.^{30,31} The brain, tumor, and segmented dural septa structures served as the basis for our finite-element model geometry.

2.2 Preoperative Computational Biomechanical Model Construction

Using the segmented brain and tumor volume, a marching cubes algorithm (followed by a decimation and surface smoothing step) was employed to establish a boundary description. A custom-built mesh generator was then used to produce a volumetric tetrahedral mesh.³² The typical brain mesh was ~84,000 tetrahedral elements and 18,000 nodes. Once constructed, displacement and pressure boundary conditions were systemically assigned to generate the subsequent atlas of volumetric displacement estimations.^{2,18,25,26,33} Specifically, the brain stem region is assigned to be fixed with no displacement. In regions associated with highest elevation when the patient's head is in the operating position, as well as within the region of the craniotomy, the brain is allowed to freely deform, i.e., stress-free condition. The remainder of the brain surface is prescribed with a displacement boundary condition that allows for tangential slip along the cranial surface but excludes normal-to-the-cranium displacements. The exact spatial designation where the stress-free and slip conditions meet is dependent on the head orientation, i.e., given a head orientation relative to gravity, an orthogonal plane based on a previously published algorithm is determined and serves as the interface.^{2,17,25,26} With respect to CSF drainage, boundary nodes above the CSF drainage level were assumed to be at an atmospheric reference pressure while boundary nodes below the CSF level were prescribed a boundary condition of no drainage, or Neumann boundary conditions set

Table 2 Patient information.

Patient #	Age and gender	Tumor type (grade)	Craniotomy diameter (cm)	Orientation	Lesion location, e.g., L/F, R/T	Lesion size (cm ³)
1	40, M	Pleomorphic xanthoastrocytoma with anaplastic features	5.5	Supine, head rotated almost 90 deg to the left	R/T	22.5
2	39, M	Oligodendroglioma (II)	3	Supine, head rotated to the right by 15 deg	L/F	87.5
3	43, M	Oligodendroglioma (II)	5	Supine, flexed slightly, rotated 45 deg to the left	R/F	84.0
4	51, F	Glioblastoma multiforme (IV)	4	Patient on right side, head further rotated to the right. Total rotation ~135 deg to the right.	L/O	90.0
5	39, F	Oligoastrocytoma (III)	7	Supine, gentle tilt, 30-deg rotation to the right	L/F	108.0
6	54, F	Metastatic adenocarcinoma	4	Supine, 45-deg rotation to the left	R/F	27.0
7	68, M	Glioblastoma multiforme (IV)	4	Supine, rotated slightly to the right	L/F	18.0
8	43, F	Astrocytoma (II)	5	Supine, 60-deg rotation to the left	R/F	15.0
9	50, M	Glioblastoma multiforme (IV)	4.5	Supine, head rotated slightly to the right	L/F	157.5

Table 3 Patient preoperative MR and iMR information.

Patient #	Preoperative MR voxel spacing	Preoperative MR sequence	iMR voxel spacing	iMR sequence
1	0.47 × 0.47 × 1.4	Ax T1 + GAD	0.94 × 0.94 × 0.90	Axial T1 Spin Echo
2	0.47 × 0.47 × 1.4	Ax 3D FSPGR + GAD	0.94 × 0.94 × 1.5	Ax T1 MPRAGE + GAD
3	0.98 × 0.98 × 1.0	Ax T1 MPRAGE + GAD	1.3 × 1.3 × 1.3	Ax T1 MPRAGE
4	0.47 × 0.47 × 1.4	Ax 3D FSPGR + GAD	1.3 × 1.3 × 1.3	Ax T1 MPRAGE + GAD
5	0.98 × 0.98 × 1.0	Ax 3D SPACE T2	0.69 × 0.69 × 2.0	Ax T2 BLADE
6	0.78 × 0.78 × 1.2	Ax 3D SPACE T2	0.69 × 0.69 × 2.0	Ax T2 BLADE
7	0.94 × 0.94 × 0.98	Ax T1 MPRAGE + GAD	1.3 × 1.3 × 1.3	Ax T1 MPRAGE + GAD
8	0.86 × 0.86 × 0.90	Ax T1 MPRAGE + GAD	0.47 × 0.47 × 1.5	Ax T1 MPRAGE + GAD
9	1.02 × 1.02 × 0.90	Ax T1 MPRAGE	0.94 × 0.94 × 0.90	Ax T1 MPRAGE

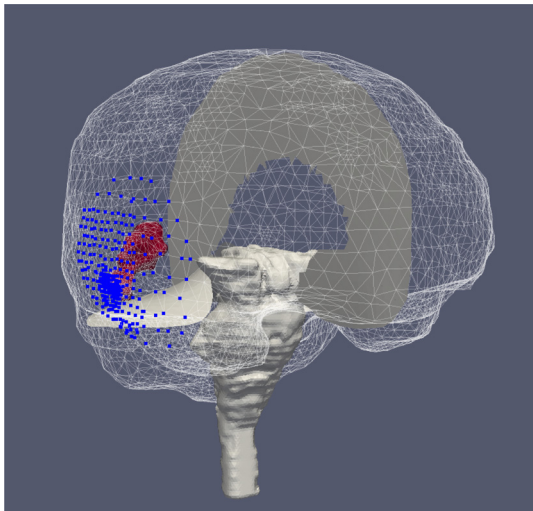


Fig. 2 Patient-specific brain mesh with atlas falx cerebri, tentorium cerebelli, and brain stem registered to patient space by applying rigid and nonrigid registrations. Approximated craniotomy nodes are in blue, and tumor volume is shown in red.

to zero. Last, regarding internal structures (falx and tentorium), slip boundary condition with no fluid drainage was assigned as the displacement and pressure boundary conditions, respectively. Given these descriptions, the mechanics-based boundary conditions will change with each head orientation, and boundary drainage conditions can change with the level of CSF drainage. These sets of variations will serve as the foundation for the description of the “atlas” below.

We should note that manual inspection of the patient’s brain mesh, brain stem, falx and tentorium representations, tumor mesh boundary, and craniotomy region were performed using Paraview³⁴ as a qualitative check on the process. Figure 2 shows an example of a computational domain.

2.3 Deformation Atlas Generation

Our brain shift compensation strategy relies on the generation of a suite of possible deformation solutions modeling gravity-

induced, osmotic-agent-induced, and swelling-induced deformations, based on numerous surgical factors, such as head orientation, CSF drainage, hyperosmotic drugs, and swelling.² To accommodate for the unpredictable and dynamic surgical environment, the aforementioned factors are perturbed such that a comprehensive and well-distributed atlas of potential deformations is provided.

More specifically, for gravity-induced shift, three different CSF drainage levels are assumed. In addition, models both with and without the presence of the space occupying lesion are also part of the atlas. This effectively represents six potential solutions for any given head orientation with respect to the direction of gravity. For osmotic-agent-induced shift, three different empirically established permeability conditions were simulated with and without the presence of the tumor, similarly providing six feasible configurations at a particular head orientation. To adjust for possible deviations from the preoperative estimation of head orientation, the model creates a cone of 60 probable head orientations, ranging ± 20 deg from the pre-operative estimation. Thus, 360 surgical presentations from gravity effects and 360 from the effects of osmotic agent on brain deformation were considered. Last, three different vascular-based solutions considering three different craniotomy sizes (75%, 100%, and 125% of the size of the planned craniotomy size) were generated to simulate brain swelling effects, yielding additional nine configurations. In summary, a total of 729 boundary condition descriptions were generated, which represent a comprehensive distribution of possible intraoperative shifts. The values of the material properties used for shift simulations can be found in Sun et al.² For each unique boundary condition set, the Galerkin method of weighted residuals was employed on the tetrahedral finite elements to resolve the partial differential equations associated with the 3-D biomechanics of brain deformation in attaining a full volumetric brain deformation solution.³⁵ The developed biphasic biomechanical model is based on Biot’s theory of consolidation and is detailed extensively in our prior work.^{2,17,25,33,36,37} We have included additional details of our constitutive biomechanical model in the Appendix. The large sparse matrix systems constructed were stored and solved using the Portable, Extensible Toolkit for Scientific Computation.³⁸

2.4 Homologous Surface Point Selection and Inverse Problem

Patient intraoperative imaging volumes were registered to the preoperative imaging data via a rigid registration based on normalized mutual information.³¹ Once again, it is important to note that the entire head volume was used for registration, rather than brain-to-brain registration to facilitate better shift measurements. Homologous cortical surface points were designated on both preoperative and registered intraoperative images using 3-D Slicer²⁸ and Analyze 9.0 (AnalyzeDirect, Overland Park, Kansas), e.g., Figs. 3(a) and 3(b). The displacements between corresponding preoperative and intraoperative surface points were used to drive the inverse problem, an example of a pair of such homologous surface points is shown in Figs. 3(a) and 3(b), in the preoperative MR imaging space and the registered iMR imaging space, respectively. Figures 3(d) and 3(e) show the surface deformation, in red vectors, from the preoperative mesh (semitransparent white) to intraoperative mesh (blue). The surface points were selected around the region of craniotomy to simulate conditions in the operating room where the exposed cortical surface would be the only source of surface information during surgery. An example of the distribution of the surface points and their spatial relation to the approximated location of the craniotomy is shown in Fig. 3(c). The objective of the inverse problem is to minimize the least squared errors between the measured surface shift and the predicted surface shift, which is a combinatory solution from the deformation atlas generated in Sec. 2.3, as shown below

$$\min \|Mw - u\|^2 \quad \exists w_i \geq 0 \quad \text{and} \quad \sum_{i=1}^m w_i \leq 1, \quad (1)$$

where M is the $r \times n$ deformation atlas, in which r represents the displacements associated with cortical surface nodes and n is the total number of solutions associated with the atlas, w are the combinatory coefficients, and u are the measured cortical surface displacements. The constraints placed on w ensure that the weighted coefficients are positive and prevent extrapolation from the existing atlas, safeguarding reasonable model-predicted deformations.²

Once the optimal combinatory fit is determined via a non-negative least squares algorithm,³⁹ the coefficients are used to extract and combine the deformations from the full volumetric atlas accordingly. Subsequently, the preoperative MR image is deformed based on the full volumetric displacement prediction via trilinear interpolation. We should note that the computational time of the initial realization of our model-based approach has been reported previously by Sun et al.² Currently, though the precomputation phase (i.e., patient-specific mesh build and deformation atlas construction) can take several hours (~ 3.4 h on average in this study), this particular phase can be computed in advance of the surgical procedure using preoperative diagnostic information (preoperative MR images and surgical planner). Moreover, intraoperative computing for model driven deformation estimation can be accomplished in near real-time (~ 1 min) with a standard desktop computer.

2.5 Subsurface Shift Measurement, Prediction, and Model Performance Assessment

After the patient's intraoperative image volume was rigidly registered to the preoperative image volume,³¹ homologous subsurface targets were selected using 3-D Slicer²⁸ and Analyze 9.0 (AnalyzeDirect, Overland Park, Kansas), a process similar to

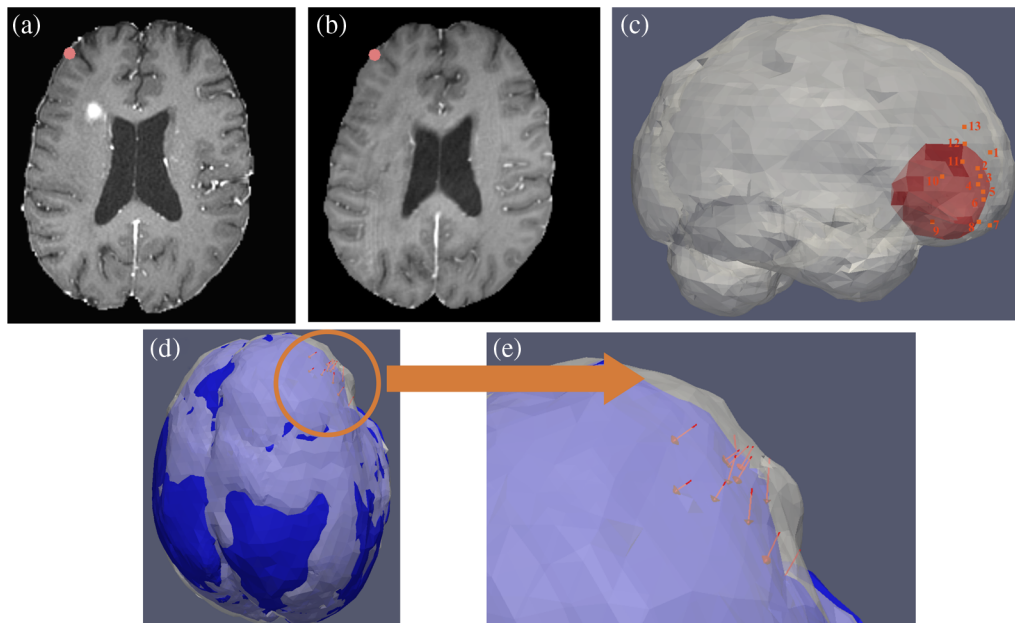


Fig. 3 Homologous surface point selection: (a) an example of a surface point selected on the preoperative MR image, (b) the corresponding surface point to (a) on the registered iMR image, (c) the distribution of surface point selections (13 points) shown on the preoperative mesh (semitransparent white), the red region represents the approximated location and size of the craniotomy, (d) the resultant vectors (red vectors) between homologous surface point selections in (a) and (b) represent the measured intraoperative surface deformation from the preoperative mesh (semitransparent white) to the intraoperative mesh (blue), and (e) a zoomed view of the surface deformation vectors in (d) from the preoperative mesh (semitransparent white) to the intraoperative mesh (blue).

the surface point selection procedure in Sec. 2.4. An example of the homologous subsurface points is shown in Fig. 4, where Fig. 4(a) shows a subsurface landmark near the tumor region on the preoperative MR image, and Fig. 4(b) shows the selected corresponding subsurface feature target on the registered iMR image. The subsurface points were selected near the tumor region, where any deformation is of greatest interest and importance to the surgeon and can have the greatest impact on clinical outcome. An example of the distribution of measured subsurface displacements around the tumor is shown in Figs. 4(c) and 4(d) in red vectors.

The identification of these subsurface targets provides measurements of actual subsurface shifts of anatomical features from preoperative-to-intraoperative space. In addition, the selected subsurface landmarks in the preoperative space can be mapped to the finite-element grid, and the model-estimated displacements, therefore, can be determined and compared. For comparison, the following were computed:

$$\vec{u}_{\text{measured}} = (x_i - x_p, y_i - y_p, z_i - z_p), \quad (2)$$

$$\vec{u}_{\text{predicted}} = (x_m - x_p, y_m - y_p, z_m - z_p), \quad (3)$$

where \vec{u} is the displacement or shift vector, x is the sagittal plane or medial–lateral axis, y is the coronal plane or anterior–posterior axis, z is the axial plane or superior–inferior axis, subscript i represents the intraoperative space, p indicates the preoperative space, and m represents the model prediction after the preoperative image is deformed.

The error of the deformation correction, e , is measured by the residual distance between subsurface intraoperative landmark

and corresponding interpolated subsurface point in model-updated image or in equation forms

$$e = \|\vec{u}_{\text{error}}\| = \|\vec{u}_{\text{predicted}} - \vec{u}_{\text{measured}}\|, \quad (4)$$

where $\|\cdot\|$ is the $L2$ norm of the vector or the Euclidean distance. The overall quality of the brain shift correction is then evaluated by percent correction, which in its equation form is

$$\text{Percent correction} = \left(1 - \frac{e}{\|\vec{u}_{\text{measured}}\|}\right) \times 100\%. \quad (5)$$

The subsurface residual error e in Eq. (4) and the percent correction of subsurface targets in Eq. (5) are the validation metrics employed in this study.

2.6 Point Selection—Measurement of Uncertainty and Propagation of Error

Since the correction algorithm is driven by homologous surface points in preoperative and intraoperative space, and the quantitative validation of our model with iMR similarly relies on the measurement between homologous subsurface points, the uncertainty in selecting corresponding intraoperative points is studied to investigate the potential window of error introduced by this manual process.

Given a distribution of preoperative feature points (surface and subsurface) in a particular case, corresponding points were identified on the intraoperative image, which were marked as point set 1. After a period of time, the same procedure was repeated to select corresponding intraoperative surface and subsurface points, given the same set of preoperative points. These

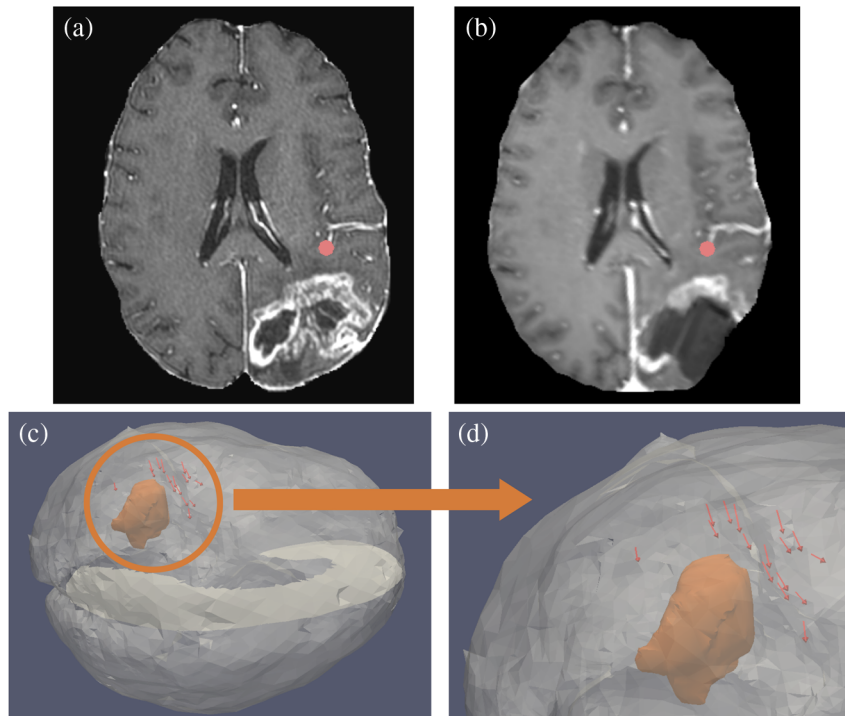


Fig. 4 Homologous subsurface point selection: (a) an example of a subsurface point selected on the preoperative MR image near the tumor region, (b) the corresponding subsurface point to (a) on the registered iMR image, (c) the distribution of subsurface displacements (red vectors) near the tumor region (in orange), and (d) a zoomed view of the subsurface displacement vectors (red), measured by subsurface homologous points.

points were labeled as point set 2. Similarly, point set 3 was acquired after another waiting period. The waiting period between selecting any two point sets ranged between 1 to 4 weeks in an effort to mitigate bias due to procedural memory.

For each point of interest, the centroid was computed from the three point sets (selections at different time points) and was treated as the ground truth. The Euclidean distances between the centroid and the manually designated point from each of the three point sets were computed, providing a measurement of uncertainty in selecting corresponding points on intraoperative image, given the same set of preoperative points. Three patient cases with considerably more identifiable surface and subsurface feature points were selected for this study.

To test the robustness of the correction algorithm, i.e., the impact on the quality of brain shift prediction due to the uncertainty in selecting homologous surface points, the inverse problem described in Sec. 2.4, was solved three times independently using each of the three intraoperative surface point sets acquired. With three unique full volumetric displacement solutions, the preoperative subsurface landmarks were interpolated to deformed image space as shown in Sec. 2.5, providing three different predictions of subsurface shifts. The predicted and measured subsurface shifts were compared to examine how the effect of uncertainty in selecting homologous surface points may propagate to the resultant volumetric deformation prediction.

3 Results

3.1 Overall View: Analysis of Nine Cases

A total of $n = 9$ patient cases were evaluated, and a total of 143 subsurface targets were identified. Of the 143 subsurface targets selected on the preoperative MR and registered iMR images, 115 subsurface displacements exceeded 3 mm, a threshold of moderate and high subsurface shift described by Bucholz et al.⁴⁰ The motivation for exclusion of shifts below 3 mm, or low shift, in this study is detailed in Sec. 4. Considering moderate and high subsurface shift only, the average measured subsurface displacement was 5.5 ± 2.6 mm. The subsurface shifts were further stratified into moderate- (between 3 and 6 mm) and high- (above 6 mm) shift groups. The stratification scheme again is based on the scale proposed by Bucholz et al.,⁴⁰ yet modified slightly to prevent substantially uneven sample sizes in the subgroups in order to facilitate comparisons. Details of the subsurface shift for nine patient cases are summarized in Table 4.

To assess the quality of the model fit, i.e., the combinatory fit drawn from the precomputed deformation atlas, the measured surface displacements, obtained by selecting homologous surface points, and model-predicted surface displacements are compared. This is an equivalent process to the analysis of subsurface shift in Sec. 2.5. The outcome of the surface correction, quantified by residual error in Eq. (4), and percent correction defined in Eq. (5) is shown in Table 5.

While the surface points alluded to in Table 5 are used to drive the inverse problem, they are not used to assess the validation performance of our model—Table 5 merely shows what could be considered a fiducial registration error for our approach. More specifically, only subsurface points were used for validation assessment in this study. The validation performance of the correction algorithm is reported in three target registration error groupings (moderate shift, high shift, and all shifts above 3 mm). The target registration error or residual error

Table 4 Subsurface shift (average shift \pm standard deviation) measured by homologous points between preoperative MR and registered iMR images.

Patient #	Measured subsurface shift (mm)		
	Moderate shift 3 to 6 mm (# of points)	High shift above 6 mm (# of points)	Moderate and high shift above 3 mm (# of points)
1	4.6 ± 0.5 (10)	7.7 ± 1.2 (3)	5.3 ± 1.5 (13)
2	4.5 ± 0.8 (13)	7.1 (1)	4.7 ± 1.0 (14)
3	4.6 ± 0.9 (15)	6.9 ± 1.0 (11)	5.6 ± 1.5 (26)
4	4.1 ± 0.7 (16)	N/A	4.1 ± 0.7 (16)
5	5.83 (1)	10.6 ± 3.3 (5)	9.8 ± 3.5 (6)
6	3.8 ± 0.4 (9)	N/A	3.8 ± 0.4 (9)
7	N/A	10.9 ± 2.7 (10)	10.9 ± 2.7 (10)
8	4.3 ± 1.0 (8)	6.3 ± 0.2 (2)	4.7 ± 1.2 (10)
9	4.0 ± 0.7 (11)	N/A	4.0 ± 0.7 (11)

Note: N/A indicates the lack of data in a particular subgroup in a patient case.

is described in Eq. (4) and percent correction defined in Eq. (5). The entirety of the target registration error and percent correction of all patients can be found in Table 6.

In further analysis of the model percent correction of the nine cases, results suggested that patient #9 could be an outlier. To address, after confirming normality using the Shapiro–Wilk test, a two-sided Grubbs' test at 5% significance level (for patient #9, $p = 0.0254 < 0.05$ or $Z_{\text{patient}\#9} = 2.236 > \text{critical value}$ of

Table 5 For surface targets: from left to right, the columns represent the patient ID, number of points used to drive the inverse problem, the average surface shift experienced in each case, and brain shift correction model performance measured in residual error and percent correction.

Patient #	Number of points	Average surface shift (mm)	Average residual surface error (mm)	Percent correction (%)
1	12	5.6 ± 0.9	2.1 ± 1.0	63.4 ± 17.9
2	10	7.1 ± 1.7	2.6 ± 1.3	63.6 ± 18.3
3	11	7.6 ± 1.3	2.9 ± 1.4	61.7 ± 18.4
4	10	6.0 ± 0.7	2.2 ± 1.2	62.6 ± 20.0
5	10	13.3 ± 3.0	3.3 ± 1.3	75.2 ± 9.8
6	7	5.9 ± 1.8	1.8 ± 1.1	69.9 ± 18.6
7	10	15.8 ± 1.5	3.8 ± 1.0	76.1 ± 6.3
8	13	6.3 ± 1.4	2.5 ± 1.0	60.2 ± 15.9
9	8	3.9 ± 1.0	2.5 ± 0.5	36.3 ± 12.8

Table 6 For subsurface targets, brain shift correction model performance measured in residual errors (average residual error \pm standard deviation of the error) and percent correction (average percent correction \pm standard deviation of percent correction).

Patient #	Moderate shift (3 to 6 mm)			High shift (>6 mm)			Moderate and high shift (>3 mm)		
	True shift (mm)	Residual error (mm)	Percent correction (%)	True shift (mm)	Residual error (mm)	Percent correction (%)	True shift (mm)	Residual error (mm)	Percent correction (%)
1	4.6	1.9 \pm 1.1	58.6 \pm 23.9	7.7	2.6 \pm 1.4	66.7 \pm 18.2	5.3	2.1 \pm 1.2	61.3 \pm 22.6
2	4.5	2.6 \pm 0.7	42.9 \pm 15.6	7.1	1.4 [*]	80.8 [*]	4.7	2.5 \pm 0.7	47.0 \pm 14.9
3	4.6	2.5 \pm 1.5	45.5 \pm 32.6	6.9	2.1 \pm 1.0	69.0 \pm 14.5	5.6	2.3 \pm 1.3	57.9 \pm 23.2
4	4.1	1.9 \pm 1.0	53.5 \pm 24.4	N/A	N/A	N/A	4.1	1.9 \pm 1.0	53.5 \pm 24.4
5	5.8	3.1 [*]	46.93 [*]	10.6	3.0 \pm 1.0	71.3 \pm 9.4	9.8	3.1 \pm 0.9	68.9 \pm 9.2
6	3.8	1.6 \pm 0.7	56.4 \pm 18.4	N/A	N/A	N/A	3.8	1.6 \pm 0.7	56.4 \pm 18.4
7	N/A	N/A	N/A	10.9	3.5 \pm 1.2	68.1 \pm 11.0	10.9	3.5 \pm 1.2	68.1 \pm 11.0
8	4.3	2.1 \pm 0.6	50.4 \pm 14.0	6.3	2.8 \pm 0.5	55.9 \pm 7.9	4.7	2.2 \pm 0.7	51.9 \pm 14.9
9	4.0	3.0 \pm 0.7	24.9 \pm 17.5	N/A	N/A	N/A	4.0	3.0 \pm 0.7	24.9 \pm 17.5

Note: N/A indicates lack of data in a particular subgroup in a patient case.

For details of subsurface shift, as well as number of points in each category, see Table 4.

^{*}Indicates only one point was present within range.

$Z = 2.215$) was performed and confirmed that patient #9 was indeed an outlier. With the identification and exclusion of patient #9 as an outlier (italics in Tables 4–6), whose exclusion is also studied in Sec. 4, the remaining eight patient cases were further analyzed to examine the model's overall performance.

3.2 Model Overall Performance Evaluation

A total of 124 subsurface targets were identified in the remaining eight patient cases. Of the 124 subsurface targets selected on the preoperative MR and registered iMR images, 104 subsurface displacements exceeded 3 mm and were considered as moderate- and high-shift targets. The overall assessment of the model's ability, excluding patient #9, to recover intraoperative brain shift is summarized in Table 7. Briefly, the residual error after correction is 2.3 ± 1.1 mm for all shifts above 3 mm (the average subsurface shift is 5.7 ± 2.6 mm in 104 targets). This translates to a percent correction of $59.0\% \pm 19.3\%$ for moderate and high shifts. Moreover, the residual error after correction for moderate shift (between 3 and 6 mm) is 2.2 ± 1.0 mm from an average subsurface shift of 4.3 ± 0.8 mm, representing $50.4\% \pm 23.3\%$ recovery, and the residual error after correction for high shift (>6 mm) is 2.8 ± 1.2 mm from an average subsurface shift of 8.8 ± 2.8 mm, representing $68.6\% \pm 13.6\%$ recovery.

The volumetric deformation introduced by the solution of the inverse problem can be observed in Fig. 5(a), where preoperative brain mesh (white semitransparent mesh) is deformed (to orange mesh) to match measured surface deformation according to Eq. (1) of Sec. 2.4. With the obtained deformation field, subsurface displacement of the preoperative target is estimated, and a comparison between measured subsurface displacement and predicted subsurface displacement is shown in Figs. 5(b) and 5(c), where red vectors represent measured subsurface displacement from preoperative MR and iMR images and blue vectors represent model predictions.

A Wilcoxon rank sum test of the distances from preoperative landmarks to corresponding intraoperative target locations before and after model correction yields $p < 0.0001$, indicating the differences resulting from the correction algorithm are statistically significant. Furthermore, a Wilcoxon rank sum test of the residual distances comparing the moderate- and high-shift group yields $p = 0.02 < 0.05$. A Wilcoxon rank sum test of the percent correction performance comparing the moderate- and high-shift group yields $p < 0.0001$. The latter two rank sum tests indicate the difference observed with respect to model performance in the moderate- and high-shift group, specifically that the model performs better in the high-shift range with greater consistency compared to in the moderate-shift group shown in Table 7, is statistically significant.

A qualitative comparison of preoperative MR images, registered iMR images, and model-updated MR images also demonstrates the impact of our brain shift correction algorithm. Examples from three different patient cases are shown in

Table 7 Overall model performance in eight cases. For subsurface targets, brain shift correction model performance measured in residual errors (average residual error \pm standard deviation of the error) and percent correction (average percent correction \pm standard deviation of percent correction).

Model overall performance in eight cases	True subsurface shift (mm) [# of points]	Residual error (mm)	Percent correction (%)
Moderate shift (3 to 6 mm)	4.3 \pm 0.8 (72)	2.2 \pm 1.0	50.4 \pm 23.3
High shift (>6 mm)	8.8 \pm 2.8 (32)	2.8 \pm 1.2	68.6 \pm 13.6
Moderate to high shift (>3 mm)	5.7 \pm 2.6 (104)	2.3 \pm 1.1	59.0 \pm 19.3

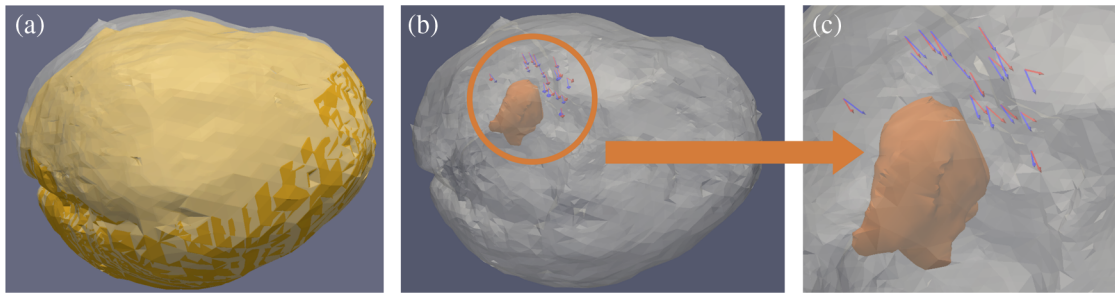


Fig. 5 (a) Deformed brain mesh resulting from the inverse problem described in Eq. (1) in Sec. 2.4. The white semitransparent mesh is generated from the preoperative MR image, and the orange mesh is the deformed mesh based on the combinatory fit that best matches the measured surface deformation and reflects the model-updated MR image, (b) comparison between the measured subsurface displacement (red vectors) between preoperative MR and registered iMR images, and the model-predicted displacement (blue vectors), and (c) a zoomed view of the measured subsurface displacement vectors (red) and model-predicted displacement (blue vectors).

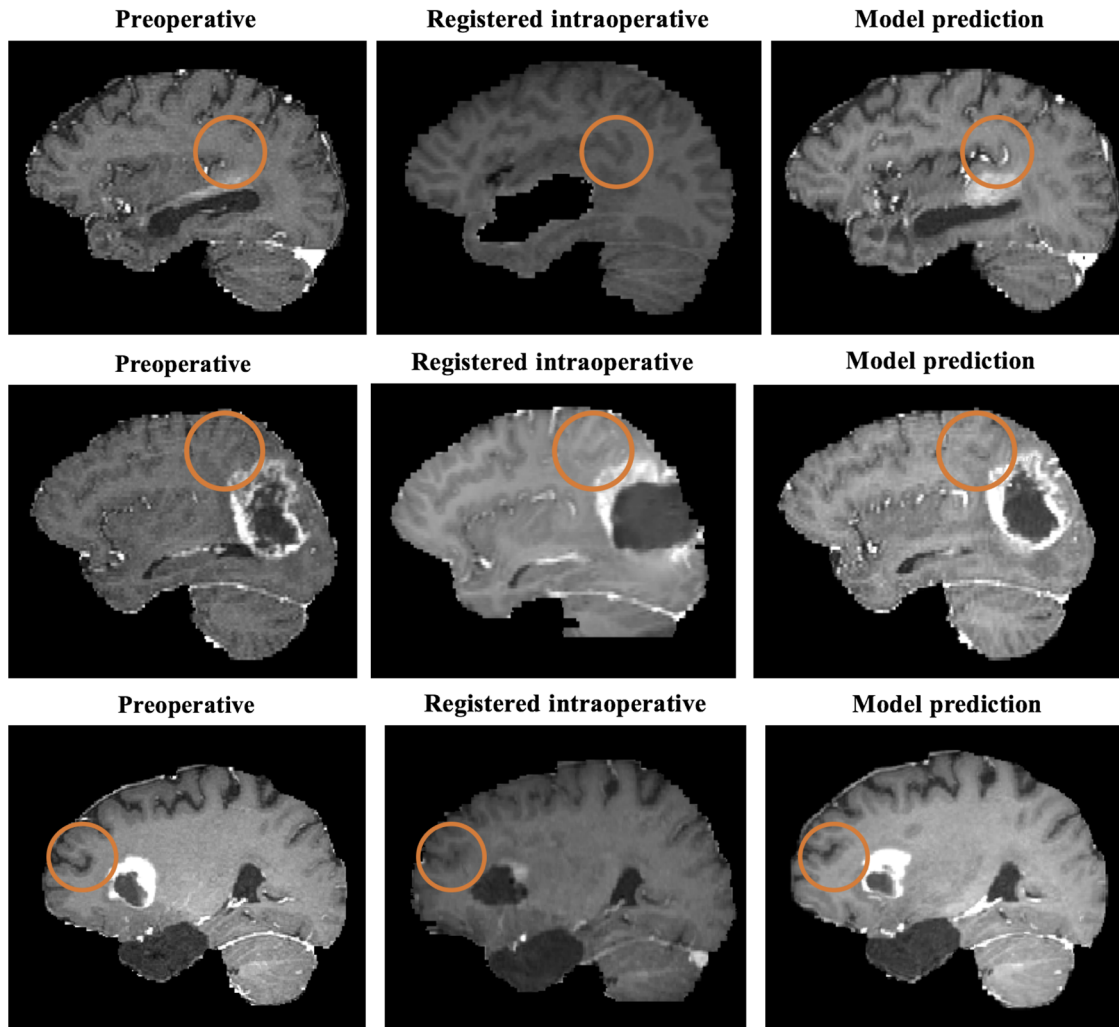


Fig. 6 Qualitative comparison of preoperative, registered intraoperative, and model-updated MR images (from left to right) in three patient cases (top to bottom: patients 1, 4, and 8) in the same spatial slice. The circles highlight features that have changed from preoperative image to intraoperative patient anatomy, yet are adequately recovered by our model-updated correction, shown in model prediction.

Table 8 Uncertainty in selecting corresponding points on iMR image volume given a set of preoperative feature points: average uncertainty in localizing corresponding intraoperative feature point \pm standard deviation of the uncertainty measured in distance from the centroid.

Patient #	Surface (mm) (# of points)	Subsurface (mm) (# of points)	All (mm) (# of points)	Friedman test p -value
1	1.1 \pm 0.5 (12)	0.9 \pm 0.4 (21)	1.0 \pm 0.5 (33)	0.18
3	1.0 \pm 0.5 (11)	0.8 \pm 0.6 (27)	0.8 \pm 0.6 (38)	0.12
4	0.7 \pm 0.5 (10)	0.7 \pm 0.3 (16)	0.7 \pm 0.4 (26)	0.11
Average	0.9 \pm 0.5 (33)	0.8 \pm 0.5 (64)	0.8 \pm 0.5 (97)	N/A

Fig. 6, where circles highlight features that have altered from preoperative imaging data to intraoperative patient anatomy (i.e., margin of contrast enhancement has changed), compared to better agreement between registered iMR image and model-updated MR image on the same slice.

3.3 Point Selection Uncertainty and Propagation of Error

A total of three cases with considerably more discernible features were analyzed to assess the uncertainty in selecting corresponding points on the intraoperative imaging volume from targets designated on the preoperative image volume. Details and motivation of this experiment can be found in Sec. 2.6. The uncertainty in point localization is quantified as the distance between a selected feature point and the centroid of the same feature point selected in three different trials. The uncertainty of all points (97 total points) across three patient cases (patients 1, 3, and 4) is 0.8 ± 0.5 mm. Specifically, the uncertainty of selecting corresponding subsurface points (64 points) on the intraoperative image volume is 0.8 ± 0.5 mm, and the uncertainty of selecting corresponding surface points (33 points) is 0.9 ± 0.5 mm. A detailed breakdown of the uncertainty in selecting homologous points on intraoperative image in each patient case can be found in Table 8. A Friedman test is performed in each patient case and the p -values are 0.18, 0.12, and 0.11 for three cases evaluated. Since all p -values are >0.05 , the threshold significance level, it is determined that the differences among three point sets in each patient case, whose selections are executed at different time points, are not statistically significant.

With three sets of intraoperative surface point selections, the volumetric deformation was calculated three different times by driving the inverse problem in each patient case. The residual errors associated with the predictions of moderate and high shift computed with three different volumetric displacement profiles are shown in Table 9 for each patient case. The largest difference of average residual errors, resulting from driving the brain shift correction with three sets of intraoperative surface point selections, is 0.07, 0.60, and 0.16 mm for patients 1, 3, and 4, respectively, indicating that an uncertainty of 0.9 ± 0.5 mm in homologous surface feature selection introduces relatively small changes in the model correction.

4 Discussion

The overarching objective of this study is to quantitatively and qualitatively assess a computational brain shift compensation strategy using iMR imaging as the comparator, the only widely accepted commercial technology available for compensating for

soft tissue changes during surgery that can resolve soft tissue heterogeneity. The findings of this study show promising results that our method can robustly predict intraoperative brain shift with sparse intraoperative surface information. The findings also encourage further prospective validation studies of our framework with active intraoperative surface deformation monitoring via stereovision or optical tracking. While improved performance is still needed, the performance of the methodology is quite promising, especially when considering the several orders of magnitude difference in cost and encumbrance imposed by iMR.

Overall, the implementation of our brain shift compensation approach reduces the subsurface brain shift from 5.7 to 2.3 mm, yielding $\sim 59\%$ brain shift correction for moderate and high subsurface shift, defined as above 3 mm. In our work, the model prediction in the high-shift range (above 6 mm) outperformed the predictions in the moderate-shift range (between 3 and 6 mm) with greater consistency, as shown in Table 7, averaging a percent correction with an impressive near 70% correction ($68.6 \pm 13.6\%$). The model correction performance is relatively consistent among eight cases analyzed, as shown in Table 6. Qualitatively, the updated MR image volume illustrates better agreement with iMR image as shown in Fig. 6 while comparing the registered preoperative image volume in this same context is less satisfying. The subsurface displacement of landmarks near the tumor is recovered well as demonstrated in Fig. 5. The localization error associated with the manual selection of homologous points was also examined. In three cases reviewed, the average uncertainty in homologous point selection among 97 surface and subsurface points was 0.8 ± 0.5 mm in Table 8. Last, the robustness of the correction algorithm was investigated to analyze the propagation of error stemming from the uncertainty in selecting homologous surface points, the driving condition of the inverse problem approach. The outcome (i.e., the residual distance) of the model correction exhibits relative indifference toward small surface selection uncertainty, as shown in Table 9.

In summary, the developed brain shift correction framework, rooted in a biomechanical biphasic model and inverse problem approach, has demonstrated a consistent performance in correcting moderate and high subsurface shift. Furthermore, the developed methodology is workflow-friendly compared to iMR imaging and has translational potential to be a complementary technology to iMR in enhancing the quality of IGNS for brain tumor resection.

While the results from eight cases analyzed show promising signs that our model-based brain shift correction framework offers an alternative and inexpensive avenue to recover brain shift intraoperatively, several limitations have affected our

Table 9 Residual error (average residual error \pm standard deviation of residual error) from average subsurface shift (average shift \pm standard deviation of shift) after the brain shift model correction driven by three different homologous surface point sets in three patients.

Patient #	Average subsurface shift (mm) above 3 mm (# of points)	Trial number	Average error for shift above 3 mm (mm)
1	5.3 \pm 1.5 (13)	1	2.1 \pm 1.2
		2	2.1 \pm 1.3
		3	2.1 \pm 1.1
3	5.6 \pm 1.5 (26)	1	2.3 \pm 1.3
		2	2.9 \pm 1.4
		3	2.4 \pm 1.3
4	4.1 \pm 0.7 (16)	1	1.9 \pm 1.0
		2	1.9 \pm 1.0
		3	2.1 \pm 0.9

model performance. The first major limitation is the model's relatively low performance in the range of low shift (below 3 mm) compared to moderate- and high-shift range. A total of 29 low shift targets were examined in our study, the model reduces the subsurface shift from 2.3 ± 0.5 mm to 1.9 ± 0.8 mm. However, the model correction in low shift range should be examined with caution. Model performance in the low shift range likely can be attributed to several reasons. First, in a three-patient study (patients 1, 3, and 4) investigating the uncertainty in selecting homologous subsurface targets, we found that the uncertainty is $\sim 0.8 \pm 0.5$ mm. Interestingly, in those same three cases, the average of low shifting subsurface targets (i.e., shift below 3 mm) was measured to be 2.1 ± 0.4 mm (9 points). This suggests that noise from point selection alone can make up as much as 38% of the subsurface shift measurement with these low shift targets. Second, and related, while the above speaks to the ability to consistently designate the same voxel, it does not address the variability in resolution of MR scans themselves (voxel size ranges can be found in Table 3), possible errors due to image distortion artifacts and potential partial-volume problems in resolving feature distinction. Last, instrumentation noise from the acquisitions of preoperative MR and iMR images, coupled with registration error when the iMR image volume is registered to the preoperative image volume for homologous point designations, can negatively impact the outcome of our brain shift correction algorithm as well. While not quantified here, a quite conservative estimate of these last two sources of error would be at least in the order of a half-voxel or ranging from 0.5 to 1.0 mm. Considering the above errors, it is likely that the measurement resolution of low shift targets is compromised. With this realization, while iMR is a powerful measurement tool, we must temper the veracity of the technology as a validation platform with our understanding of how the error of our comparator may influence our quantitative analysis.

Exploring this last aspect further, the lack of a true gold standard in quantifying the accuracy of model-based shift correction

is certainly a limitation. Groups have used both nonlandmark metrics and landmarks for validation, as discussed in Table 1. Using nonlandmark metrics, such as the 3-D bounds of ventricles by Joldes et al.²² or modified Hausdorff distance from extracted edge maps by Vigneron et al.,²³ is a reasonable approach to alleviate the concerns of subjective error in landmark selection. However, the drawbacks of these metrics are: (1) the metric of Joldes et al.²² does not provide reliable indications on the model performance outside of an arbitrarily designated anatomical structure, which is often remote from the surgical target and (2) the metric of Vigneron et al.²³ has dependency on the adjustable parameters of Canny edge detection method. Other groups have used landmarks to evaluate their model-based methods, namely, Skrinjar et al.,¹⁹ Ferrant et al.,²⁰ and Zhang et al.,²¹ detailed in Table 1. Our comparison study with iMR has similarly used landmarks for assessment. However, different from Ferrant et al.²⁰ and Zhang et al.,²¹ the selection of validation targets in our study has attempted to only identify subsurface landmarks in the vicinity of the tumor region. The rationale behind our selection strategy is: (1) landmarks on the cortical surface may provide biased assessments on the performance of model-based approaches, as most of the model-based methods also use intraoperative surface data as a driving force of the model—Ferrant et al.²⁰ report that the best accuracy produced by their model is for landmarks located on the boundary surfaces (including the cortical surface), and the worst accuracy is obtained near tumor and resection regions.²⁰ A similar trend was observed in our study, the model performance in correcting brain shift on the surface, as shown in Table 5, generally exceeds the performance with subsurface validation targets near the tumors as shown in Tables 6 and 7. (2) While placing landmarks in both hemispheres in Ferrant et al.²⁰ or extracting edge maps of the whole brain in Vigneron et al.²³ provides valuable metrics assessing the performance of the model-based approaches globally, landmarks in the vicinity of the tumor region have the most significant and immediate effect on the localization of the tumor region and the assessment of tumor margins intraoperatively and, therefore, directly impact the outcome and safety of the surgery.^{20,23} Last, as shown in Table 1, the limited number of patient cases and landmarks continues to be a challenge for validation studies of model-based brain shift correction framework. Hence, further exploration and study should be carried out regarding the development of better validation metrics, ideally with less subjective human influence and with a more targeted region of interest near the tumor.

The third considerable limitation in the work reported herein is the challenging task of sampling preoperative and intraoperative surface points. Although we have attempted to quantify the uncertainty in localizing homologous points and find that our algorithm is relatively insensitive to small uncertainties of homologous surface point selection, the task of manually finding features on the surfaces of preoperative MR and iMR images remains difficult. For example, as in Sec. 2.4, the surface points are often selected near the region of craniotomy to mimic a realistic operating room (OR) environment; however, the selections of surface points did sometimes fall outside of the designated craniotomy area due to lack of features on the iMR images, which currently are acquired after surgical resection, as shown in Fig. 7. The issue of the occasional lack of features on the surface extends to subsurface point selection near the tumor region as well. Tables 4 and 5 provide summaries of

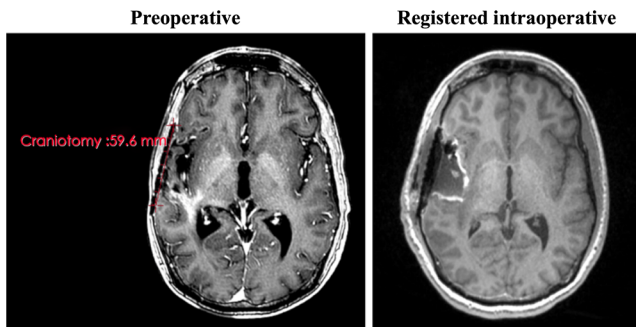


Fig. 7 An example illustrating the lack of available surface features near the craniotomy region on iMR image.

the number of surface and subsurface points selected for this comparison study with iMR and further demonstrate that the availability of homologous surface and subsurface points varies from case to case due to a number of factors, such as the quality of the iMR images (described in Table 3) and the nature of the surgical procedure itself. However, the problem of identifying features on iMR imaging volume acquired after resection can be mitigated by a more active and continuous surface deformation monitoring technique during procedures, which is an area of active investigation.

For example, some investigators have considered the deployment of laser range scanner (LRS), documented by Miga et al.⁴¹ as well as Sinha et al.⁴² and subsequently adopted by Zhang et al.²¹ A second approach uses stereovision systems that are embedded with neurosurgical microscopes, reported by Kumar et al.⁴³ and Ji et al.⁴⁴ The advantages of employing active intraoperative monitoring methods, LRS or stereovision, to obtain surface deformation are: (1) surface displacement acquired via these active monitoring techniques is better spatially and temporally resolved than iMR measurements, (2) the cortical surface is feature rich and offers more dense measurements, and (3) in the case of stereovision, is extremely workflow-friendly. Undoubtedly these two noncontact approaches have their own challenges. The LRS acquisition time, including the positioning of the apparatus and scanning, can take up to 4 min, which can be a limitation in providing temporally dense digitization of the cortical surface for intermediate updates.^{2,43} The stereovision approach, designed to overcome the deficiencies of temporal resolution of LRS data, may be implemented using stereo cameras (1) externally mounted onto the operating microscope in Sun et al.⁴⁵ and Ji et al.⁴⁴ or (2) internal to the microscope in Kumar et al.⁴³

The challenges associated with the application of stereovision include the accuracy of calibration, lighting conditions in the OR, as well as difficulties in establishing continuous stereo correspondence due to significant surgical events, such as bleeding, or unexpected incidents, such as disturbance or obstruction (e.g., surgeon's gloves) in the field of view.^{43–45}

Also, while not emphasized herein, the use of intraoperative ultrasound (iUS) should not be neglected as an intraoperative sparse data source for driving brain shift correction methodologies. A study by Morin et al.⁴⁶ has attempted to perform brain shift correction by registering blood vessels and cortical surface from preoperative data to iUS data using a constraint-based biomechanical simulation. Subsequently, the preoperative MR imaging data can be updated volumetrically via the deformation field produced in the previous step.⁴⁶ While demonstrating promises as a valuable method in acquiring intraoperative surface and subsurface brain shift measurements in Reinertsen et al.³ and Morin et al.,⁴⁶ iUS has its own challenges of limited volume extent, operator dependency, imaging artifacts, such as from intraoperative bleeding, the possibility of introducing additional shift as it is a contact method, as well as probe calibration^{47,48} (though regarding this last item, an interesting study by Chen et al.⁴⁹ was recently reported that suggests sub-millimeter tracking accuracy may be possible with iUS).

One last note, there are certainly aspects of our brain shift correction model that can be improved. For example, currently our model accounts for resection by decoupling the nodes associated with the segmented tumor volume during the assembly of the stiffness matrix.^{26,50} However, in patient #9, a case that was deemed a statistical outlier and excluded from overall model performance assessment, we observed a collapsed resection cavity that our model was unable to capture, and the subsurface shift near the tumor was not resolved as well as desired. From Table 5, it is shown that when eight homologous surface points were selected on the preoperative MR and iMR image volumes, the average surface shift is 3.9 ± 1.0 mm, which is the smallest surface shift among all nine cases examined. When subsurface deformation is examined, as shown in Figs. 8(a)–8(c), the direction of the subsurface deformation shows a strong tendency to collapse into the tumor.

To quantify this observed “debulking,” the centroid of the tumor volume was computed, and the vector between each preoperative subsurface target and the centroid of the tumor was obtained, i.e., the debulking direction. The corresponding measured subsurface deformation (where only shift above 3 mm is considered, as discussed previously) is represented as the “measured” direction. The dot product between debulking and measured unit vectors

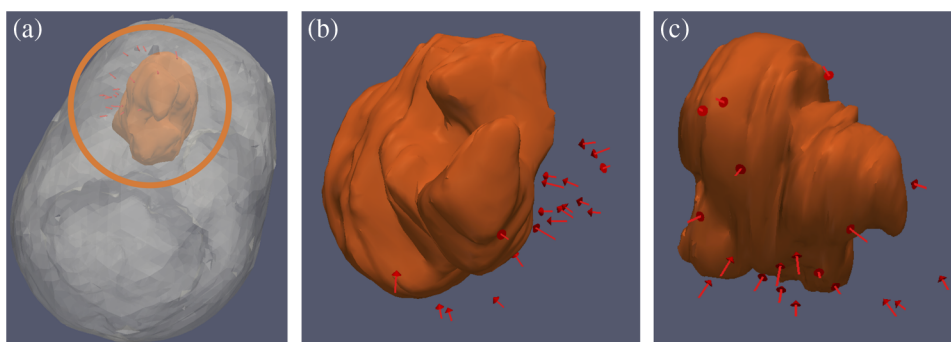


Fig. 8 Patient #9: (a) subsurface deformation in red vectors near the tumor, (b) and (c) present different views of the subsurface deformation vectors (red) in patient #9, illustrating a collapsed resection cavity.

exhibits a larger average magnitude of 0.95 ± 0.06 , i.e., a smaller directional difference ($14.5 \text{ deg} \pm 11.0 \text{ deg}$) between the measured deformation vector and the debulking direction, compared to the model-predicted deformation vector and the debulking direction (dot product: 0.72 ± 0.23 or $40.8 \text{ deg} \pm 19.9 \text{ deg}$), further confirming the visual observation of a collapsed resection cavity in Fig. 8. It should also be noted that the average subsurface deformation for moderate- and high-shift targets for this case is $4.0 \pm 0.7 \text{ mm}$, making it the only case that the average surface shift is less than average subsurface shift. A case of small surface deformation coupled with strong resection cavity collapse is a scenario that our model, in its current implementation, does not mechanically account for well and illustrates the need to build on our existing mechanism to better account and compensate for resection effect in our model.

5 Conclusion

This paper reports a comparison study of a biphasic biomechanical model-based brain shift correction framework with a current clinically available comparator, iMR imaging. It demonstrates that our model-based methodology, with a patient-specific computational inverse problem approach, can compensate for a considerable extent of brain shift during tumor resection via sparse intraoperative surface deformation information with minimal disruptions to the existing clinical workflow and infrastructure in the operating room. While showing that our approach is a promising complementary technology to iMR to account for brain shift in IGNS procedures and standard brain tumor resection cases, more validation is still warranted. As this study indicates, conducting these evaluations is quite challenging, and systematic approaches to reduce measurement and validation assessment errors are needed. Nevertheless, this work provides important steps forward in validating computational strategies to reduce intraoperative brain shift error.

Appendix: Computational Model Details

The biomechanical model implemented in our deformation atlas-based brain shift corrections strategy is a biphasic model based on Biot's theory of consolidation, which describes the mechanical behavior of a poroelastic medium via equations of linear elasticity for the solid matrix and Darcy's law for fluid flow through the porous matrix.^{17,33,36,51,52} Given its biphasic nature, Biot's consolidation theory was used to model the deformation behavior of the brain. Specifically, equations below were used to describe the deformation behavior of the brain^{2,17,36}

$$\nabla \cdot G \nabla \vec{u} + \nabla \frac{G}{1-2\nu} (\nabla \cdot \vec{u}) - \alpha \nabla p = -(\rho_t - \rho_f)g, \quad (6)$$

$$\alpha \frac{\partial}{\partial t} (\nabla \cdot \vec{u}) + k_c(p - p_c) + \nabla \cdot (-k \nabla p) = 0, \quad (7)$$

where G is the shear modulus, \vec{u} is the displacement vector, ν is the Poisson's ratio, α is the ratio of the extracted fluid volume and volume change of the tissue under compression, p is the interstitial pressure, ρ_t is the tissue density, ρ_f is the fluid density, g is the gravitational vector, t is time, k_c is the capillary permeability, p_c is the intracapillary pressure, and k is the hydraulic conductivity.

In our constitutive model, briefly, Eq. (6) represents the equation of mechanical equilibrium. In Eq. (6), deformations may be introduced from interstitial fluid pressure gradient, surface forces, and displacements, as well as changes to tissue buoyancy forces.²⁶ Particularly, the right-hand side of Eq. (6) is used to simulate the effect of gravitational forces on the brain—intraoperative CSF drainage decreases the buoyancy, thus causing the brain to sag.^{26,33} Equation (7) relates the time rate of change of the volumetric strain of the solid matrix to the changes in hydration.^{2,17,26,36} Moreover, Eq. (7) allows for dilatation effects or the fluid exchange between capillary and interstitial spaces, due to osmotically active drugs.^{2,17,26,36}

Disclosures

No conflicts of interest, financial or otherwise, are declared by the authors.

Acknowledgments

This work was supported by the National Institute for Neurological Disorders and Stroke of the National Institutes of Health under Grant No. R01NS049251, the National Center for Image Guided Therapy under Grant No. P41EB015898, and the National Cancer Institute under Grant No. K25CA204599.

References

1. C. Nimsky et al., "Quantification of, visualization of, and compensation for brain shift using intraoperative magnetic resonance imaging," *Neurosurgery* **47**(5), 1070–1080 (2000).
2. K. Sun et al., "Near real-time computer assisted surgery for brain shift correction using biomechanical models," *IEEE J. Transl. Eng. Health Med.* **2**, 2500113 (2014).
3. I. Reinertsen et al., "Intra-operative correction of brain-shift," *Acta Neurochir.* **156**(7), 1301–1310 (2014).
4. I. J. Gerard et al., "Brain shift in neuronavigation of brain tumors: a review," *Med. Image Anal.* **35**, 403–420 (2017).
5. C. Delorenzo et al., "Image-guided intraoperative cortical deformation recovery using game theory: application to neocortical epilepsy surgery," *IEEE Trans. Med. Imaging* **29**(2), 322–338 (2010).
6. D. L. G. Hill et al., "Measurement of intraoperative brain surface deformation under a craniotomy," *Neurosurgery* **43**(3), 514–526 (1998).
7. N. Hamzé et al., "Anticipation of brain shift in deep brain stimulation automatic planning," in *37th Annual Int. Conf. of the IEEE Engineering in Medicine and Biology Society (EMBC)*, pp. 3635–3638 (2015).
8. A. L. Simpson et al., "Evaluation of conoscopic holography for estimating tumor resection cavities in model-based image-guided neurosurgery," *IEEE Trans. Biomed. Eng.* **61**(6), 1833–1843 (2014).
9. E. Uhl et al., "Intraoperative computed tomography with integrated navigation system in a multidisciplinary operating suite," *Neurosurgery* **64**(5), 231–239 (2009).
10. J. M. K. Mislav, A. J. Golby, and P. M. Black, "Origins of intraoperative MRI," *Neurosurg. Clin. North Am.* **20**(2), 137–146 (2009).
11. C. Nimsky et al., "Intraoperative high-field-strength MR imaging: implementation and experience in 200 patients," *Radiology* **233**(1), 67–78 (2004).
12. C. Senft et al., "Intraoperative MRI guidance and extent of resection in glioma surgery: a randomised, controlled trial," *Lancet Oncol.* **12**(11), 997–1003 (2011).
13. C. Schulz, S. Waldeck, and U. M. Mauer, "Intraoperative image guidance in neurosurgery: development, current indications, and future trends," *Radiol. Res. Pract.* **2012**, 197364 (2012).
14. C. DeLorenzo et al., "Volumetric intraoperative brain deformation compensation: model development and phantom validation," *IEEE Trans. Med. Imaging* **31**(8), 1607–1619 (2012).

15. I. Reinertsen et al., "Vessel driven correction of brain shift," in *Medical Image Computing and Computer-Assisted Intervention (MICCAI 2004)*, Vol. 3217, pp. 208–216 (2004).
16. S. J. Chen et al., "Validation of a hybrid Doppler ultrasound vessel-based registration algorithm for neurosurgery," *Int. J. Comput. Assisted Radiol. Surg.* **7**(5), 667–685 (2012).
17. P. Dumpuri et al., "A fast and efficient method to compensate for brain shift for tumor resection therapies measured between preoperative and postoperative tomograms," *IEEE Trans. Biomed. Eng.* **57**(6), 1285–1296 (2010).
18. I. Chen et al., "Integrating retraction modeling into an atlas-based framework for brain shift prediction," *IEEE Trans. Biomed. Eng.* **60**(12), 3494–3504 (2013).
19. O. Skrinjar, A. Nabavi, and J. Duncan, "Model-driven brain shift compensation," *Med. Image Anal.* **6**(4), 361–373 (2002).
20. M. Ferrant et al., "Serial registration of intraoperative MR images of the brain," *Med. Image Anal.* **6**(4), 337–359 (2002).
21. C. Zhang, M. Wang, and Z. Song, "A brain-deformation framework based on a linear elastic model and evaluation using clinical data," *IEEE Trans. Biomed. Eng.* **58**(1), 191–199 (2011).
22. G. R. Joldes et al., "Real-time prediction of brain shift using nonlinear finite element algorithms," in *Medical Image Computing and Computer-Assisted Intervention—MICCAI 2009: 12th International Conference, London, UK, September 20–24, 2009, Proceedings, Part II*, G.-Z. Yang et al., Eds., pp. 300–307, Springer Berlin Heidelberg, Berlin, Heidelberg (2009).
23. L. M. Vigneron et al., "Enhanced FEM-based modeling of brain shift deformation in image-guided neurosurgery," *J. Comput. Appl. Math.* **234**(7), 2046–2053 (2010).
24. M. I. Miga et al., "Clinical evaluation of a model-updated image-guidance approach to brain shift compensation: experience in 16 cases," *Int. J. Comput. Assist. Radiol. Surg.* **11**(8), 1467–1474 (2016).
25. I. Chen et al., "Intraoperative brain shift compensation: accounting for dural septa," *IEEE Trans. Biomed. Eng.* **58**(3), 499–508 (2011).
26. P. Dumpuri et al., "An atlas-based method to compensate for brain shift: preliminary results," *Med. Image Anal.* **11**(2), 128–145 (2007).
27. U. M. Upadhyay and A. J. Golby, "Role of pre- and intraoperative imaging and neuronavigation in neurosurgery," *Expert Rev. Med. Devices* **5**(1), 65–73 (2008).
28. A. Fedorov et al., "3D Slicer as an image computing platform for the quantitative imaging network," *Magn. Reson. Imaging* **30**(9), 1323–1341 (2012).
29. P. A. Yushkevich et al., "User-guided 3D active contour segmentation of anatomical structures: significantly improved efficiency and reliability," *NeuroImage* **31**(3), 1116–1128 (2006).
30. G. K. Rohde, A. Aldroubi, and B. M. Dawant, "The adaptive bases algorithm for intensity-based nonrigid image registration," *IEEE Trans. Med. Imaging* **22**(11), 1470–1479 (2003).
31. F. Maes et al., "Multimodality image registration by maximization of mutual information," *IEEE Trans. Med. Imaging* **16**(2), 187–198 (1997).
32. J. M. Sullivan, G. Charron, and K. D. Paulsen, "A three-dimensional mesh generator for arbitrary multiple material domains," *Finite Elem. Anal. Des.* **25**(3–4), 219–241 (1997).
33. M. I. Miga et al., "Model-updated image guidance: initial clinical experiences with gravity-induced brain deformation," *IEEE Trans. Med. Imaging* **18**(10), 866–874 (1999).
34. J. Ahrens, B. Geveci, and C. Law, *ParaView: An End-User Tool for Large Data Visualization Handbook*, Elsevier, San Diego, California (2005).
35. D. R. Lynch, *Numerical Partial Differential Equations for Environmental Scientists and Engineers: a First Practical Course*, Springer, New York (2005).
36. K. D. Paulsen et al., "A computational model for tracking subsurface tissue deformation during stereotactic neurosurgery," *IEEE Trans. Biomed. Eng.* **46**(2), 213–225 (1999).
37. D. W. Roberts et al., "Intraoperative brain shift and deformation: a quantitative analysis of cortical displacement in 28 cases," *Neurosurgery* **43**(4), 749–758 (1998).
38. S. Balay et al., "Efficient management of parallelism in object-oriented numerical software libraries," in *Modern Software Tools for Scientific Computing*, E. Arge, A. M. Bruaset, and H. P. Langtangen, Eds., pp. 163–202, Birkhäuser Boston, Boston, Massachusetts (1997).
39. C. Lawson and R. Hanson, *Solving Least Squares Problems*, Society for Industrial and Applied Mathematics, Prentice-hall, Inc., Englewood Cliffs, New Jersey (1974).
40. R. D. Bucholz et al., "The correction of stereotactic inaccuracy caused by brain shift using an intraoperative ultrasound device," in *CVRMed-MRCAS'97: First Joint Conference—Computer Vision, Virtual Reality and Robotics in Medicine and Medical Robotics and Computer-Assisted Surgery*, Vol. 1205, pp. 459–466 (1997).
41. M. I. Miga et al., "Cortical surface registration for image-guided neurosurgery using laser-range scanning," *IEEE Trans. Med. Imaging* **22**(8), 973–985 (2003).
42. T. K. Sinha et al., "A method to track cortical surface deformations using a laser range scanner," *IEEE Trans. Med. Imaging* **24**(6), 767–781 (2005).
43. A. N. Kumar et al., "Persistent and automatic intraoperative 3D digitization of surfaces under dynamic magnifications of an operating microscope," *Med. Image Anal.* **19**(1), 30–45 (2015).
44. S. Ji et al., "Cortical surface shift estimation using stereovision and optical flow motion tracking via projection image registration," *Med. Image Anal.* **18**(7), 1169–1183 (2014).
45. H. Sun et al., "Stereopsis-guided brain shift compensation," *IEEE Trans. Med. Imaging* **24**(8), 1039–1052 (2005).
46. F. Morin et al., "Brain-shift compensation using intraoperative ultrasound and constraint-based biomechanical simulation," *Med. Image Anal.* **40**, 133–153 (2017).
47. S. Bayer et al., "Intraoperative imaging modalities and compensation for brain shift in tumor resection surgery," *Int. J. Biomed. Imaging* **2017**, 6028645 (2017).
48. M. Ivanov et al., "Intraoperative ultrasound in neurosurgery—a practical guide," *Br. J. Neurosurg.* **24**(5), 510–517 (2010).
49. E. C. S. Chen, T. M. Peters, and B. Ma, "Guided ultrasound calibration: where, how, and how many calibration fiducials," *Int. J. Comput. Assisted Radiol. Surg.* **11**(6), 889–898 (2016).
50. M. I. Miga et al., "Modeling of retraction and resection for intraoperative updating of images," *Neurosurgery* **49**(1), 75–84 (2001).
51. M. A. Biot, "General theory of three-dimensional consolidation," *J. Appl. Phys.* **12**(2), 155–164 (1941).
52. A. Hagemann et al., "Biomechanical modeling of the human head for physically based, nonrigid image registration," *IEEE Trans. Med. Imaging* **18**(10), 875–884 (1999).

Ma Luo received his BS degree in bioengineering from the University of Pittsburgh in 2015. He is a PhD student in the Department of Biomedical Engineering at Vanderbilt University. His research interests are in computational modeling and inverse problem for biomedical applications, particularly brain stimulation.

Sarah F. Frisken is a researcher in computer graphics, shape representation, medical image processing and scientific visualization. She is an inventor of adaptively sampled distance fields, a graphical shape representation that has wide application ranging from fonts and digital drawing to 3D sculpting. Her work is used commercially in Saffron, a font rendering system used by Adobe Flash and Monotype, in Mischief, a digital drawing system sold by The Foundry, and in high end milling simulation.

Prashin Unadkat is a postdoctoral researcher in the Surgical Planning Laboratory at Brigham and Women's Hospital, Harvard Medical School having previously completed his medical school training at K. J. Somaiya Medical College in Mumbai, India. His research focuses on image guidance for neurosurgery and surgical brain mapping.

Alexandra J. Golby is a neurosurgeon and director of image-guided neurosurgery at Brigham and Women's Hospital in Boston and a professor of neurosurgery and professor of radiology at Harvard Medical School. Her clinical practice is devoted to surgery for brain tumors and other lesions, especially those involving critical brain regions. Her research focuses on functional and molecular brain mapping using

a variety of emerging technologies to guide neurosurgical planning and intraoperative decision making.

Michael I. Miga received his PhD in biomedical engineering from Dartmouth College in 1998. He joined Vanderbilt University in Spring of 2001 and is the Harvie Branscomb professor at Vanderbilt. He is a professor of biomedical engineering, radiology,

and neurological surgery. He is the Biomedical Modeling Laboratory director and cofounder of the Vanderbilt Institute for Surgery and Engineering. His research interests are in computational modeling and inverse problems for therapeutic applications and imaging.

Biographies for the other authors are not available.